Astronomical Techniques and Instruments, Vol. 2, July 2025, 265–273

Article Open Access

# Research on the accurate calculation method of crater position in lunar surface images based on feature matching

**Yanning Zheng[1,2], Xue Dong[1,2*], Zhipeng Liang[1,2], Jian Gao[1], Bowen Guan[1], Liyan Sun[1], Xingwei Han[1,2], He Dong[3*]**

[1]*Changchun Observatory*, *National Astronomical Observatories*, *Chinese Academy of Sciences*, *Jilin* 130117, *China*

[2]*University of Chinese Academy of Sciences*, *Beijing* 100049, *China*

[3]*College of Information Technology*, *Jilin Normal University*, *Jilin* 136000, *China*

*Correspondences: dongx@cho.ac.cn; donghe@jlnu.edu.cn

Received: March 4, 2025; Accepted: March 13, 2025; Published Online: April 29, 2025; https://doi.org/10.61977/ati2025026; https://cstr.cn/32083.14.ati2025026



Citation: Zheng, Y. N., Dong, X., Liang, Z. P., et al. 2025. Research on the accurate calculation method of crater position in lunar surface images based on feature matching. *Astronomical Techniques and Instruments*, **2**(4): 265−273. https://doi.org/10.61977/ati2025026.

**Abstract:** Lunar Laser Ranging has extremely high requirements for the pointing accuracy of the telescopes used. To improve its pointing accuracy and solve the problem of insufficiently accurate telescope pointing correction achieved by tracking stars in the all-sky region, we propose a processing scheme to select larger-sized lunar craters near the Lunar Corner Cube Retroreflector as reference features for telescope pointing bias computation. Accurately determining the position of the craters in the images is crucial for calculating the pointing bias; therefore, we propose a method for accurately calculating the crater position based on lunar surface feature matching. This method uses matched feature points obtained from image feature matching, using a deep learning method to solve the image transformation matrix. The known position of a crater in a reference image is mapped using this matrix to calculate the crater position in the target image. We validate this method using craters near the Lunar Corner Cube Retroreflectors of Apollo 15 and Luna 17 and find that the calculated position of a crater on the target image falls on the center of the crater, even for image features with large distortion near the lunar limb. The maximum image matching error is approximately 1″, and the minimum is only 0.47″, which meets the pointing requirements of Lunar Laser Ranging. This method provides a new technical means for the high-precision pointing bias calculation of the Lunar Laser Ranging system.

**Keywords:** Lunar Laser Ranging system; High-precision pointing correction; Lunar surface features; Image feature matching; Deep learning; Crater position calculation

## 1. INTRODUCTION

Lunar exploration is essential for studying the Moon and utilizing its resources, and lays important groundwork for the establishment of lunar bases and further deep space exploration. The robotic probes undertaking lunar exploration require core scientific support, such as accurate lunar orbital parameters and lunar reference frames, to ensure that exploration missions are optimally executed. Although China's lunar exploration has achieved world-renowned results, there are still areas that require more work to match other international agencies in technical fields such as Lunar Laser Ranging (LLR). LLR is a technology for precisely measuring the Earth-Moon distance that, especially with the application of the next-generation single solid Lunar Corner Cube Retroreflectors (LCCRs), an optical device installed on the Moon's surface to reflect Earth-based laser beams, is expected to reach millimeter-level observation accuracy[1–3]. LLR data play a crucial role in the fields of astronomical geodynamics, lunar physics, general relativity, and studies on the Earth-Moon reference frame, providing a strong scientific basis for the exploration of the Earth-Moon system and the Moon's internal structure[4–6].

Laser ranging systems inevitably yield pointing errors due to mechanical processing, installation, gravity, and temperature changes[7]. The distance between the Earth and the Moon is approximately 380000 km, and a pointing bias of 1″ from the ground towards the Moon is equivalent to a distance error of 1.86 km on the lunar surface. The Luna 17 LCCR, because of its uncertain location, acquired only a small amount of valid data in the early stages of its placement and was then "lost" until 2010, when high-resolution images taken by the Lunar Reconnaissance Orbiter Camera (LROC) helped reposition Lunokhod 1 and valid observational data from Luna 17

were regained. It is worth noting that the new estimated coordinates of Luna 17 differ from the original estimated coordinates by approximately 5 km[8], which corresponds to a pointing bias of only about 3″ from the ground station. In addition, the number of laser ranging echo photons is inversely proportional to the fourth power of the distance, and the number of effective echo photons that can be received is very limited for LLR systems[9,10]. Consequently, telescope pointing accuracy is even more important for LLR[11], making it a key factor affecting the success of any observations taken.

Telescope pointing error correction is usually achieved by tracking dozens of stars in the all-sky region, obtaining the amount of stellar pointing bias and modeling the pointing error, thereby achieving pointing bias correction for the telescope[12,13]. Although this method improves the integrated pointing accuracy of the telescope in the all-sky region, the bias of a specific pointing may still be too large, negatively impacting LLR observations. Meanwhile, with the accumulation of telescope operation time and seasonal changes, a previously devised pointing model may no longer be applicable, leading to a further decrease in pointing accuracy that would seriously compromise the accuracy of the LLR system.

To meet the pointing accuracy requirements for LLR, we devise a processing scheme to calculate and correct the current pointing bias of the telescope in real time. Given the small size of the LCCR and the large Earth-Moon distance, it is difficult for the ground camera to accurately capture its shape. To alleviate this, we suggest using a larger crater near the LCCR as a reference feature to calculate pointing bias. Because telescope pointing bias varies very little over a small range of azimuth and altitude changes, the pointing deviation calculated based on the crater can be directly applied to the corresponding LCCR. Accurately obtaining the position of craters in the image is the key to determining pointing bias. Crater images on the lunar surface can be distorted because of the observation angle, lunar surface topography, lighting conditions and other factors. Traditional crater recognition techniques rely on edge detection to extract features[14–17], but they do not currently show satisfactory performance. Deep learning techniques have shown continuous progress, prompting them to be applied to crater recognition[18–22], however, these methods mainly focus on the recognition of craters in the orthographic projection view, and focus on determining whether a region in the image is a crater and its approximate contour, rather than pinpointing the positional coordinates of the crater in the image. To solve this problem, our proposed method for accurately calculating lunar crater positions uses lunar surface feature matching. The method solves the transformation matrix between the feature points by matching the common feature points between the reference image and the target image. It then accurately calculates the exact location of the crater in the target image using the transformation matrix and known crater location information in the reference image. The effectiveness and accuracy of feature matching are ensured because of the uniqueness of lunar craters and their surrounding geomorphological features such as mountain ranges, hills, and rift valleys.

## 2. MATERIALS AND METHODS

Image matching is a technique that can identify and establish corresponding relationships between similar structures in two or more images. Feature-based image matching algorithms are fast, stable and computationally efficient, and typically include three stages: feature point detection, feature point description, and feature point matching[23,24]. Early image matching techniques relied primarily on manually determined features, acquired using bespoke algorithms that extract local or global characteristics from images, to represent their key information. These algorithms include Scale Invariant Feature Transform (SIFT)[25], Speeded Up Robust Features (SURF)[26], Oriented FAST and Rotated BRIEF (ORB)[27], which usually rely on pre-determined structures, meaning the accuracy may be unreliable for complex scenery or under adverse lighting conditions. With the rapid development of deep learning technology, the field of image matching has also seen significant progress, and numerous advanced methods based on deep learning have emerged that outperform traditional methods used to determine feature positions and other non-deep-learning methods on image matching datasets. Standout examples of these are SuperPoint[28] and SuperGlue[29], the developers of which have performed a comparative analysis with traditional methods to verify the superior performance of their algorithms. Here, we use the SuperPoint and SuperGlue algorithms for feature matching in lunar surface images.

### 2.1. SuperPoint and SuperGlue Algorithms

SuperPoint and SuperGlue are two important algorithms for feature point detection and matching, and their core processes are shown in Fig. 1. The SuperPoint algorithm uses a full convolutional neural network to achieve keypoint detection and description in a self-supervised learning framework. SuperGlue is a neural network that uses an attention mechanism to jointly search for correspondences, eliminating non-matching points by aggregating contextual information. This achieves efficient matching between two sets of local features.

As shown in Fig. 2[28], the SuperPoint architecture is a full convolutional neural network that performs on full-size images, using descriptors for interest point detection. The model consists of an input, shared encoder, interest point detection decoder, interest point description decoder, and output. The shared encoder is used to process and reduce the dimensionality from $H \times W$ to $H/8 \times W/8$ of the input image. The interest point detection decoder finds the interest points based on the weights of the task, and the $\chi \in R^{(H/8)\times(W/8)\times 65}$ is computed by interest point detector head. After passing through Softmax and Reshape, a tensor sized $H \times W$ is output. Another decoder performs the description of the interest points, and a tensor sized $H \times W \times D$ is output after passing through Bi-Cubic Interpo-

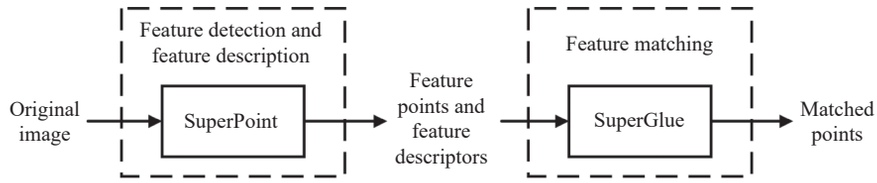


**Fig. 1. The image matching processes of the SuperPoint and SuperGlue algorithms.**

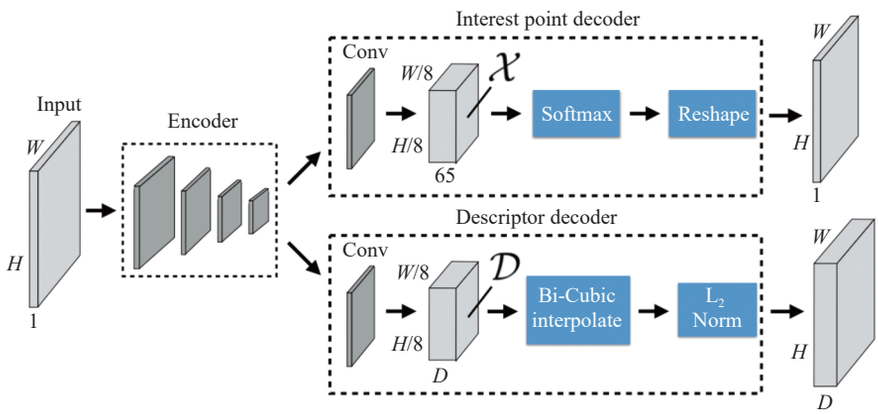


**Fig. 2. The network architecture of SuperPoint consists of a shared encoder and two parallel decoders for interest point detection and descriptor extraction.**

late and $L_2$ Norm. For the detection and description of interest points, traditional methods have a processing order in which detection is followed by description, whereas SuperPoint network parameters enable sharing between the detection and description tasks to generate interest points and descriptors simultaneously.

SuperGlue comprises two main parts: The Attention Graph Neural Network and the Optimal Match Layer (shown in Fig. 3[29]). The Attention Graph Neural Network takes feature points $\boldsymbol{p}$ and their descriptors $\boldsymbol{d}$ as inputs, which are processed into a single vector by the Keypoint Encoder module. Subsequently, the attention intersection network layer carries out multiple iterations to generate richer matching descriptors $\boldsymbol{f}$. The Optimal Matching Layer finds optimal allocation using the Sinkhorn Algorithm for $T$ iterations.

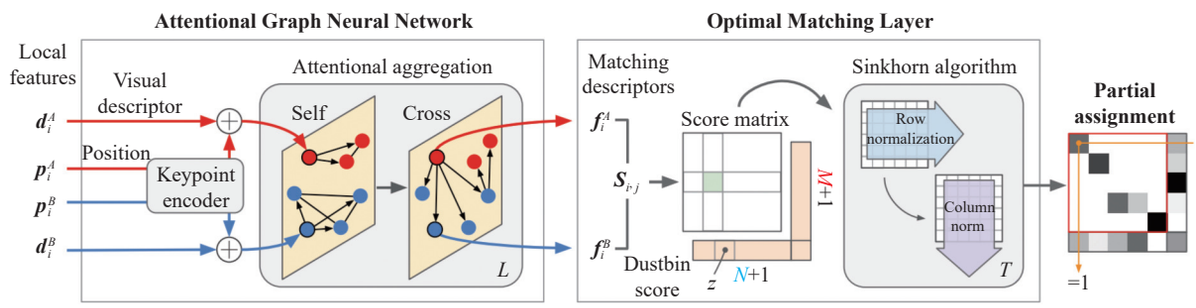


**Fig. 3. The network architecture of SuperGlue consists of an Attention Graph Neural Network and the Optimal Match Layer.**

SuperPoint and SuperGlue are robust to external factors such as shape change and light change. Through self-supervised learning, SuperPoint is able to stably detect keypoints in different visual environments, while SuperGlue uses its attention mechanism and contextual information to improve matching quality and maintains high accuracy even under challenging conditions, meeting the stringent requirements of lunar surface feature matching.

## 2.2. Creation of a Reference Image Library

The image field of view used in this paper has a size of 3′, and based on the mean Earth-Moon distance and the lunar diameter, the distance range of the lunar surface covered by the 3′ field of view corresponds to approximately 10% of the lunar diameter. The images of the lunar surface used in the study were taken from the NASA SVS (Scientific Visualization Studio) website[30]. SVS has modeled lunar phase changes and libration effects on the Moon at hourly intervals using LROC images, with corresponding atlases available for download. The reference image of the lunar surface used in this paper was taken from this atlas, and the 3′ field of view is over an image size of 282 × 282 pixels, with each pixel corresponding to 0.6383″. The theoretical locations of the craters in the reference image are acquired from Lunar QuickMap[31], powerful web application for data exploration and analysis that provides detailed lunar surface information such as crater names and coordinates.

Lunar QuickMap uses imagery from LROC[32], which has an image resolution of up to 0.5 m/pixel[33]. Meanwhile, the Lunar QuickMap tool can provide a scale with a maximum resolution of 10 m[31], which is equivalent to a pointing deviation of 1/180″ (shown in Fig. 4). For these reasons, the Lunar QuickMap data best meet the LLR requirements.

The lunar surface features and the visual integrity of the crater can change significantly because of varying lighting conditions, and this must be taken into account when constructing a reference image set. In this study, we classify the Moon's terminator line into seven cases according to its position in relation to the selected craters (shown in Fig. 5): Near Evening Line (NEL), Small Area in the Night Region (SANR), Large Area in the Night Region (LANR), Small Area in the Light Region (SALR), Large Area in the Light Region (LALR), Near Morning Line (NML), and Moon Daytime (MDT). The details of the cases are shown in Table 1.

## 2.3. Image Transformation and Crater Position Calculation

A homography is a mapping between any two images of the same planar surface acquired separately[34], and it can handle geometric transformations in images such as rotation, scaling, translation, and perspective. As discussed in Section 2.1 we can match the feature points between the reference image (*Ref_Img*) and the target image (*Target_Img*), and then use these points to solve the corresponding homography transformation matrix[35].

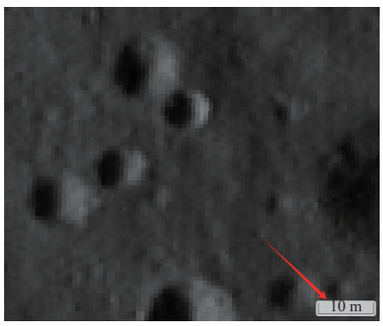


**Fig. 4. A sample image of the lunar surface, demonstrating that the maximum resolution of the QuickMap scale is 10 m, which is equivalent to a pointing deviation of 1/180″.**

The homography transformation is represented by a 3 × 3 matrix $\boldsymbol{H}$ for mapping a point $\boldsymbol{X}$ in one image plane $\Pi$ to a point $\boldsymbol{X}'$ in another image plane $\Pi'$, as shown in Fig. 6. This transformation can be expressed as

$$\boldsymbol{X}' = \boldsymbol{H}\boldsymbol{X} \Leftrightarrow \begin{bmatrix} x' \\ y' \\ \omega' \end{bmatrix} = \begin{bmatrix} h_{11} & h_{12} & h_{13} \\ h_{21} & h_{22} & h_{23} \\ h_{31} & h_{32} & h_{33} \end{bmatrix} \begin{bmatrix} x \\ y \\ \omega \end{bmatrix}, \quad (1)$$

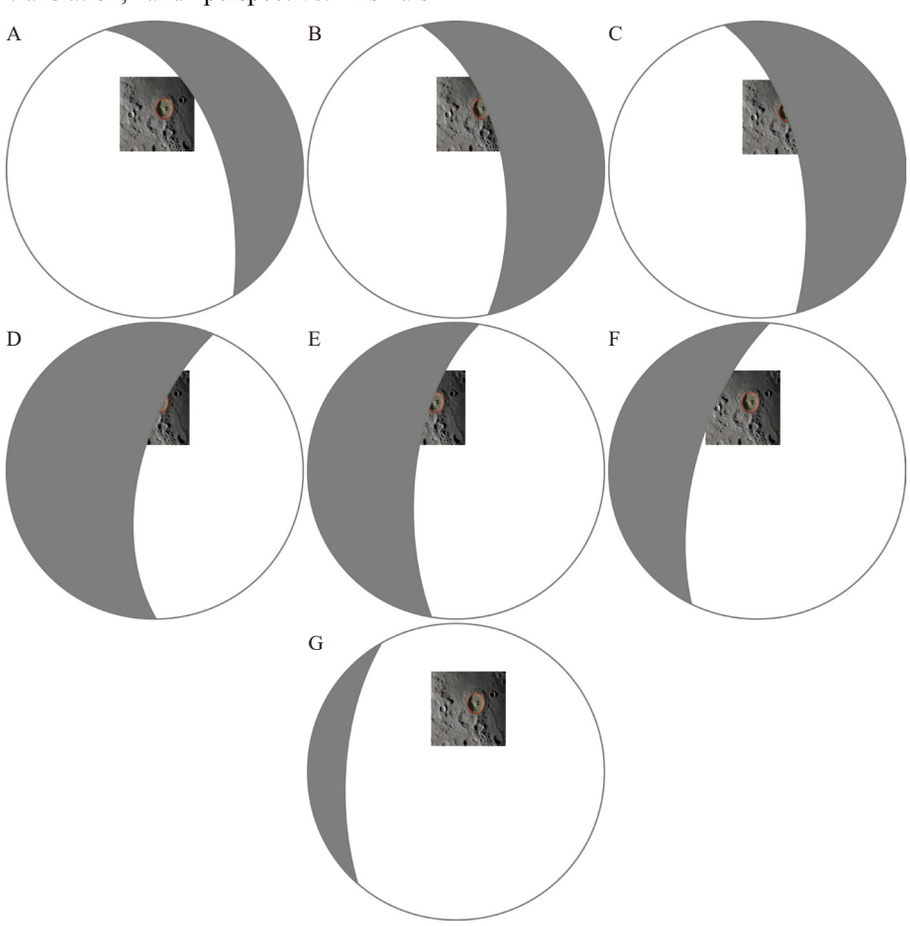


**Fig. 5. Position of the reference image in relation to the Moon's terminator line.** (A) NEL. (B) SANR. (C) LANR. (D) SALR. (E) LALR. (F) NML. (G) MDT.

**Table 1. Sample number and sample distribution for each case**

| Case | Sample number | Sample distribution |
|---|---|---|
| NEL | 5 | ● Crater shadow is at the edge of the crater.<br>● Crater shadow takes up approximately ¼ of the crater.<br>● Crater shadow takes up approximately ½ of the crater.<br>● Crater shadow takes up approximately ¾ of the crater.<br>● Crater shadow completely fills the crater. |
| SANR | 1 | Approximately ⅓ of the crater is within the Night Region. |
| LANR | 1 | Approximately ⅔ of the crater is within the Night Region. |
| SALR | 1 | Approximately ⅓ of the crater is within the Light Region. |
| LALR | 1 | Approximately ⅔ of the crater is within the Light Region. |
| NML | 5 | ● Crater shadow completely fills the crater.<br>● Crater shadow takes up approximately ¾ of the crater.<br>● Crater shadow takes up approximately ½ of the crater.<br>● Crater shadow takes up approximately ¼ of the crater.<br>● Crater shadow is at the edge of the crater. |
| MDT | 3 | ● Between MDT-B and NML-A.<br>● The crater is most strongly illuminated by the sun.<br>● Between MDT-B and NEL-A. |

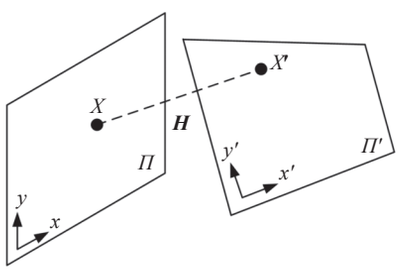


**Fig. 6. Image coordinates are transformed using a homography matrix.**

where $h_{11}$, $h_{12}$, ... , $h_{33}$ are matrix elements, $\boldsymbol{X}$ and $\boldsymbol{X'}$ are homogeneous coordinates, and in general $\omega' = \omega = 1$. Using the homography transformation matrix $\boldsymbol{H}$, it is possible to achieve the transformation of the reference image, including the craters within the image. The transformed reference image is denoted as *Ref_Img*_1.

The reference image library mentioned in Section 2.2 contains 7 images, and the target image needs to be feature-matched with these reference images one by one. The number of matching points is an important indicator to measure the similarity between two images. A higher number of matching points results in the features of the two images being more coincident, indicating a higher degree of similarity and more reliable matching.

The accuracy and validity of the matching results can be quantified by the matching precision; with higher precision, the accuracy of the match becomes more secure. We adopt the Root Mean Square Error (RMSE) of the matching point coordinates as an evaluation metric for the precision of the matching points, given by

$$RMSE = \sqrt{\frac{1}{m}\sum_{j=1}^{m}\left[\left(x'_j - \hat{x}_j\right)^2 + \left(y'_j - \hat{y}_j\right)^2\right]}, \qquad (2)$$

where $m$ is the number of matched points, $j$ is the index of the matched point, $\left(x'_j, y'_j\right)$ is the coordinates of the $j$-th matching point on *Ref_Img*_1, and $\left(\hat{x}_j, \hat{y}_j\right)$ is the coordinates of the $j$-th matching point on *Target_Img*.

To screen out the reference image that best fits the target image, we construct a scoring mechanism based on the number of matching points and matching accuracy, as shown in Equation (3). In this mechanism, the level of the score directly reflects the confidence of the match between the reference image and the target image, and the higher the score, the higher the confidence of the match. The matching score of the $i$-th reference image, $Score_i$, is calculated as

$$Score_i = \frac{\min\left(RMSE_1, RMSE_2, \cdots, RMSE_n\right)}{RMSE_i} + \frac{m_i}{\max\left(m_1, m_2, \cdots, m_n\right)}, \qquad (3)$$

where, $n$ is the number of images in the reference image set, $i$ is the reference image index, $m_i$ is the number of matching points between the $i$-th reference image and the target image, and $RMSE_i$ is the matching accuracy obtained from the $i$-th reference image and the target image.

The index $k$, corresponding to the maximum value of the score, is

$$k = \arg\max\left(Score_i\right), \quad 1 \leqslant i \leqslant n. \qquad (4)$$

The steps for solving the crater coordinate in the target image are as follows:

(1) Feature matching. The *Ref_Img* and the *Target_Img* are input into SuperPoint, and the output feature points and descriptors are used as input for SuperGlue to output the matched points.

(2) Image transformation. The matched points are used to solve for the homography transformation matrix $\boldsymbol{H}$ between *Ref_Img* and *Target_Img*. Matrix $\boldsymbol{H}$ is applied to transform *Ref_Img* and get *Ref_Img*_1. At the same time, matrix $\boldsymbol{H}$ is applied to convert the coordinates of the craters in the reference image and record the transformed coordinates.

(3) Secondary feature matching. The SuperPoint and

SuperGlue algorithms perform feature detection and matching on *Ref_Img*_1 and *Target_Img*, the transformation matrix $\boldsymbol{H}$ is calculated, the number of matched points $m$ is recorded, and the *RMSE* of the matched point coordinates is calculated.

(4) Calculate scores and select the best reference image. All reference images are analyzed iteratively, repeating steps 1 to 3, and the score of each matching is calculated according to Equation (3). The reference image with the highest score is then determined.

(5) Determine the coordinates of the craters in the target image. After selecting the best reference image, to improve the matching accuracy, multiple iterations of matching and transformation are performed, based on the results of step 3, until the RMSE converges. The coordinates of the crater obtained from the last transformation correspond to the position of the crater in the target image.

## 3. RESULTS AND DISCUSSION

To verify the validity and general applicability of our proposed method, we select images of the crater Aristillus near the Apollo 15 reflector and the crater Bianchini near the Luna 17 reflector under different light conditions and carry out validation experiments. Bianchini, being close to the lunar limb, shows significant variation in visible lunar surface features, while Aristillus, located in a more central region of the Moon, has more regular shapes. The matching of the image features and the determination of the crater locations for Aristillus and Bianchini are shown in Fig. 7 and Fig. 8, respectively. There are significant differences between the reference and target images in terms of location, angle, and lighting conditions before feature matching. After feature matching and transformation of the reference image by translation, rotation, scaling, and other transformations through the transformation matrix, the obtained images are highly compatible with the target images, and the calculated crater positions fall precisely on the center of the corresponding crater positions on the target images, proving the validity of the crater position coordinates.

The accuracy of the image feature matching points for Aristillus and Bianchini under different lighting conditions is given in Table 2. As discussed in Section 2.2, one pixel in the image corresponds to 0.6383″, and the maximum RMSE value is 1.583 pixels, equivalent to approximately 1″, while the minimum value is only 0.735 pixels, equivalent to 0.47″. The RMSE is the integrated error of pixel coordinates, and its correlation with the telescope's integrated pointing accuracy can be analyzed in terms of the effect on the telescope's azimuth axis and elevation axis. When the matching error comes only from the image height direction, it only affects the telescope's elevation axis, and the pointing accuracy of the elevation axis is equal to the matching error. When the matching error comes only from the image width direction, it only affects the telescope's azimuth axis, and the pointing accuracy of the azimuth axis is equal to the matching error divided by the cosine of the current elevation angle. Considering a telescope with an elevation axis of 60° as an example, the integrated pointing accuracy results are shown in Table 3. When lighting conditions are poor and the lunar surface feature distortions are severe, the calculation accuracy of the telescope's pointing error is at its worst at 2″ (see Table 2 and Table 3). With good image conditions, the calculation accuracy of the telescope's pointing error is less than 1″, with a minimum value of approximately 0.5″, which meets the pointing requirement for LLR and further confirms the validity of the calculated crater positions. It also demonstrates the robustness and accuracy of the image feature matching method, which maintains good computational accuracy even in the presence of large distortion of image features present at the lunar limb.

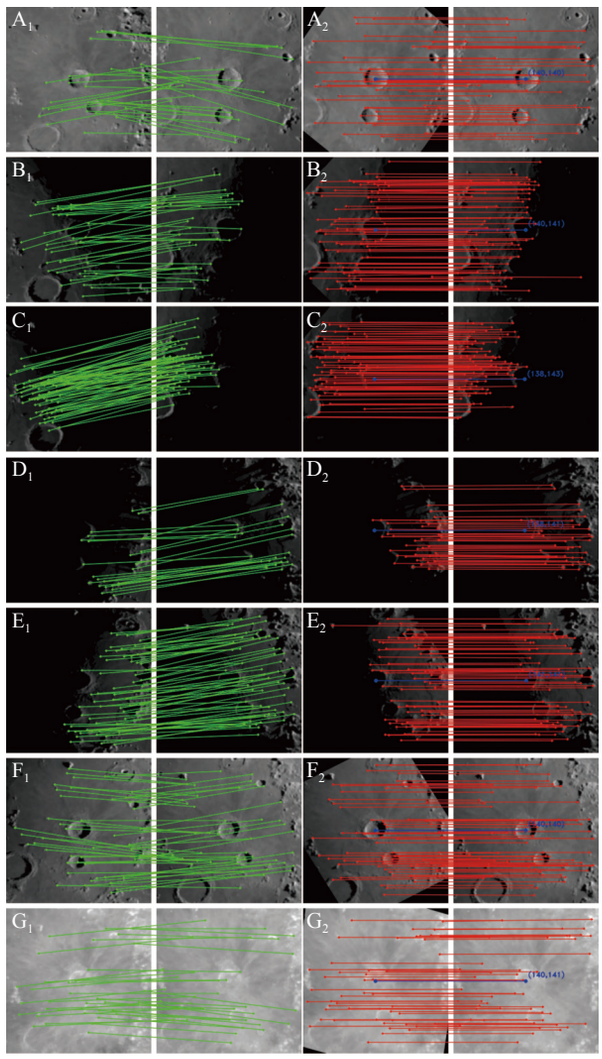


**Fig. 7. Feature matching and position calculation of lunar crater Aristillus. Columns A–G correspond to the classification of A–G in Section 2.2. $A_1$–$G_1$ are the matches between the reference image (left) filtered by the score and the target image (right), and $A_2$–$G_2$ are the matches between the reference image (left) transformed by the homography matrix and the target image (right).**

Each target image is matched with all the reference

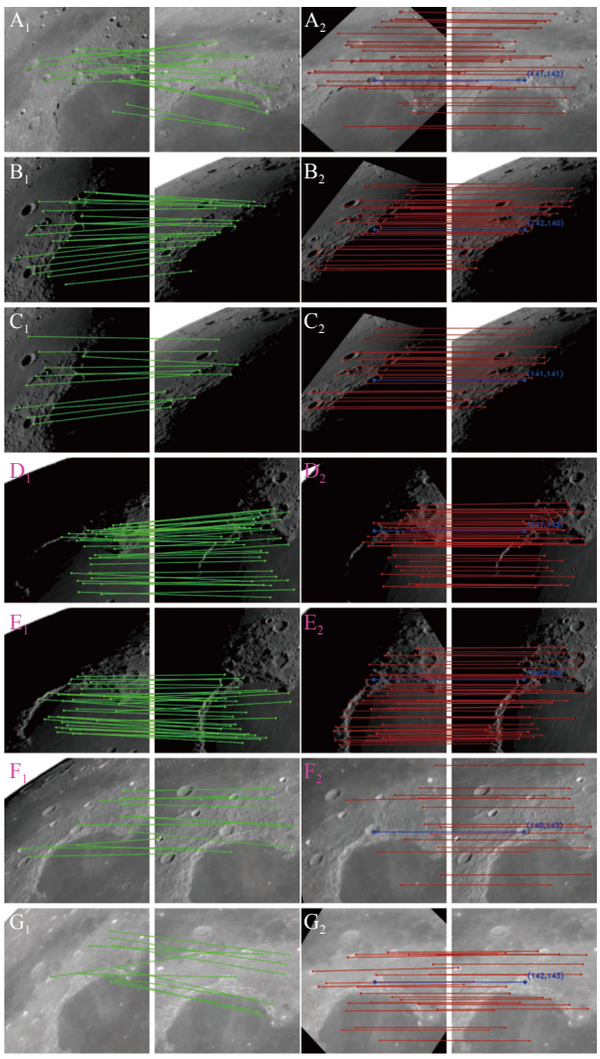


**Fig. 8. Feature matching and position calculation of lunar crater Bianchini. Columns A−G correspond to the classification of A−G in Section 2.2. $A_1$−$G_1$ are the matches between the reference image (left) filtered by the score and the target image (right), and $A_2$−$G_2$ are the matches between the reference image (left) transformed by the homography matrix and the target image (right).**

images, the best match is filtered, and the crater position is calculated. The runtime of the program is shown in Table 4. The basic process of pointing correction for the telescope is to stop tracking the current LCCR, switch to the target crater, wait for the telescope tracking to stabilize, take a photo of the lunar surface feature, calculate the position of the crater in the image, calculate the telescope pointing bias, stop tracking the crater, and continue to track the original LCCR and carry out the observation based on the correction of the pointing bias. The whole pointing correction process is time-consuming, and the time taken by the lunar surface feature matching program is acceptable for it. The program can be further optimized to enhance its operational efficiency.

The matching points do not appear in the dark areas of the lunar surface images (see Fig. 7 and Fig. 8), and the feature matching points exist only in the light areas. Combined with the accuracy data in Table 2, when the dark areas of a lunar surface image account for a large proportion, the matching process becomes a local matching rather than whole-image matching, resulting in a decrease in the matching accuracy of the image. Therefore, when selecting the lunar surface features near the LCCR, it is advisable to choose areas with the largest possible illuminated area to increase the distribution ratio of feature points, so as to improve matching accuracy. In addition, using the classification method in Section 2.2, the accuracy of the classification can be further refined according to the light conditions, especially the three categories of NEL, NML, and MDT. This refinement aims to expand the sample size of the reference image library, ensuring that the target image can be matched with a more appropriate reference image, thereby improving the accuracy of the calculated coordinates of lunar craters in the target image.

Another point we would like to discuss is an overall scheme for applying our proposed methodology to LLR systems. During the LLR process, factors such as the environmental temperature and telescope altitude angle change over time, causing temperature, gravity, and other factors to affect the telescope pointing. To ensure the pointing accuracy of the telescope, pointing corrections need to be performed periodically (at intervals typically in the range of 15−20 min) when no valid data are captured. The LLR system is driven locally by the software used for our proposed method. When the telescope pointing correction is needed, the LLR control system guides the telescope to track a given crater on the lunar surface. When the telescope tracking is stable, a camera is used to take an image of the lunar surface, and the position of the crater in the image is calculated. Then, the off-target amount of

**Table 2. Matching accuracy of images under different lighting conditions in pixels**

| Crater | NEL | SANR | LANR | SALR | LALR | NML | MDT |
|---|---|---|---|---|---|---|---|
| Aristillus | 0.934 | 1.301 | 1.475 | 1.253 | 0.828 | 0.735 | 0.880 |
| Bianchini | 1.435 | 1.583 | 1.174 | 1.479 | 1.384 | 1.511 | 0.986 |

**Table 3. Telescope integrated pointing accuracy corresponding to image matching error at an example altitude of 60°**

| Matching error/(″) | All bias on elevation/(″) | All bias on azimuth/(″) | The same on azimuth and elevation/(″) |
|---|---|---|---|
| 1.00 | 1.00 | 2.00 | 1.58 |
| 0.47 | 0.47 | 0.94 | 0.74 |

**Table 4. Statistics on the running time of the program to complete an image matching process in seconds**

| Crater | NEL | SANR | LANR | SALR | LALR | NML | MDT |
|---|---|---|---|---|---|---|---|
| Aristillus | 3.52 | 3.17 | 2.95 | 3.24 | 3.29 | 3.43 | 3.37 |
| Bianchini | 3.47 | 3.36 | 3.31 | 2.89 | 3.02 | 3.39 | 3.25 |

the crater coordinates is calculated based on the crater position in the image and the theoretical position. Finally, based on this off-target amount, the telescope pointing bias is calculated and sent to the LLR control system for pointing correction.

## 4. CONCLUSION

Here, we conceptualize a processing scheme for calculating the pointing bias of an LLR system based on lunar craters. To accurately calculate the position of craters in lunar surface images, we propose a precise method for crater position calculation based on lunar feature matching. This method detects and matches common feature points between reference and target images using the deep learning algorithms SuperPoint and SuperGlue to solve for the transformation matrix between these feature points. It then uses this matrix to calculate the position of craters in the target image.

We also design a scoring mechanism to select the best-matching reference image from a reference image library. Experiments conducted with craters near the Apollo 15 and Luna 17 reflectors show that the crater coordinates calculated by the proposed method fall on the center of the craters in the target image, with the maximum image matching error being about 1″ and the minimum as low as 0.47″. This demonstrates good computational accuracy. Theoretically, the integrated pointing error of the telescope after correction by this method is approximately 1″, meeting the pointing requirements for LLR.

We also find that selecting lunar surface features with larger illuminated areas near the LCCR can increase the distribution proportion of feature points in the image, which is expected to improve the matching accuracy. Additionally, the computational accuracy of the lunar crater coordinates in the target image may be further enhanced by refining the classification of reference images and expanding the sample size of the reference image library to match the target image with more suitable reference images. To verify these speculations, future research will require more in-depth analytical demonstrations and experiments.

## ACKNOWLEDGMENTS

This research was funded by Natural Science Foundation of Jilin Province (20220101125JC), and the National Natural Science Foundation of China (12273079).

## AI DISCLOSURE STATEMENT

AI-assisted technology is not used in the preparation of this work.

## AUTHOR CONTRIBUTIONS

Yanning Zheng conceived the ideas, implemented the study, and wrote the paper. Xue Dong, Xingwei Han and He Dong performed manuscript review editing and mentoring. Zhipeng Liang and Jian Gao made suggestions for the optimization of the methodology. Bowen Guan and Liyan Sun conducted the screening and categorization of the experimental data. All authors read and approved the final manuscript.

## DECLARATION OF INTERESTS

The authors declare no competing interests.

### REFERENCES

[1] Huang, K., Yang, Y. Z., Tang, R. F., et al. 2024. Review of the development of Lunar Laser Ranging. *Astronomical Techniques and Instruments*, **1**(6): 295−306.

[2] He, Y., Hu, Z. Z., Li, M., et al. 2021. Schematic design of new generation of Lunar corner cube retroreflector with single aperture. *Journal of Deep Space Exploration*, **8**(4): 416−422. (in Chinese)

[3] Porcelli, L., Currie, D. G., Muccino, M., et al. 2021. Next Generation Lunar Laser Retroreflectors for fundamental physics and Lunar science. NASA. Goddard Space Flight Center.

[4] Müller, J., Murphy, T. W., Schreiber, U., et al. 2019. Lunar Laser Ranging: a tool for general relativity, lunar geophysics and Earth science. *Journal of Geodesy*, **93**(11): 2195−2210.

[5] Hua, Y., Huang, C. L. 2012. On the observation and research of Lunar Laser Ranging. *Process in Astronomy*, **30** (3): 378−393. (in Chinese)

[6] Biskupek, L., Singh, V. V., Müller, J., et al. 2022. Benefit of improved Lunar Laser Ranging data for the determination of Earth orientation parameters. In Proceedings of the International Workshop on Laser Ranging.

[7] Huang, B. L., Han, X. E., Zhang, N., et al. 2014. Axis correction of satellite laser ranging system based on image processing technique. *Laser & Infrared*, **44**(7): 715−719. (in Chinese)

[8] Jr. Murphy, T. W., Adelberger, E. G., Battat, J. B. R., et al. 2011. Laser ranging to the lost Lunokhod 1 reflector. *Icarus*, **211**(2): 1103−1108.

[9] Li, Y. Q., Fu, H. L., Li, R. W., et al. 2019. Research and experiment of Lunar Laser Ranging in Yunnan Observatories. *Chinese Journal of Lasers*, **46**(1): 188−195. (in Chinese)

[10] He, Y., Liu, Q., Tian, W., et al. 2017. Study on Laser Ranging for satellite on the second Lagrange Point of Earth-Moon system. *Journal of Deep Space Exploration*, **4**(2): 130−137. (in Chinese)

[11] Luck, J. 2004. Mount model stability. In Proceedings of 14th International Workshop on Laser Ranging.

[12] Zhang, X. X., Wu, L. D. 2001. The basic parameters of telescope static point model. *Acta Astromomica Sinica*, **42** (2): 198−205. (in Chinese)
[13] Xie, Y. M., Zhao, Y. L. 2010. Telescope pointing error analysis and correction method research of satellite laser ranging. *Optics & Optoelectronic Technology*, **8**(3): 89−92. (in Chinese)
[14] Sawabe, Y., Matsunaga, T., Rokugawa, S. 2006. Automated detection and classification of Lunar Craters using multiple approaches. *Advances in Space Research*, **37**(1): 21−27.
[15] Cheng, Y., Johnson, A. E., Matthies, L. H., et al. 2003. Optical landmark detection for spacecraft navigation. In Proceedings of 13th AAS/AIAA Space Flight Mechanics Meeting.
[16] Feng, J. H., Cui, H. T., Cui, P. Y., et al. 2010. Autonomous crater detection and matching on planetary surface. *Acta Aeronautica et Astronautica Sinica*, **31**(9): 1858−1863. (in Chinese)
[17] Zhang, W. M., Zhang, X. B., Li, Q. Z., et al. 2013. Automatic crater extraction method for lunar images under low solar elevation angle. *Journal of Astronautics*, **34**(9): 1246−1252. (in Chinese)
[18] Chen, D., Hu, F., Zhang, L. Q., et al. 2024. Impact crater recognition methods: A review. *Science China Earth Sciences*, **67**(6): 1719−1742.
[19] Liu, Y. S., Lai, J. L., Xie, M. G., et al. 2024. Identification of lunar craters in the Chang'e-5 landing region based on Kaguya TC morning map. *Remote Sensing*, **16**(2): 344.
[20] Jia, Y. T., Wan, G., Liu, L., et al. 2020. Automated detection of lunar craters using deep learning. In Proceedings of 2020 IEEE 9th Joint International Information Technology and Artificial Intelligence Conference (ITAIC).
[21] Wang, S., Fan, Z. Z., Li, Z. M., et al. 2020. An effective lunar crater recognition algorithm based on convolutional neural network. *Remote Sensing*, **12**(17): 2694.
[22] Silburt, A., Ali-Dib, M., Zhu, C. C., et al. 2019. Lunar crater identification via deep learning. *Icarus*, **317**: 27−38.
[23] Huang, K., Yang, H. 2024. Review of deep-learning-feature-based methods for 2D image matching. *Computer Engineering*, **50**(10): 16−34.
[24] Xu, M. Y., Liu, W. B., Zheng, X. A., et al. 2022. Image feature matching method based on deep learning. *Transducer and Microsystem Technologies*, **41**(7): 61−64. (in Chinese)
[25] Lowe, D. G. 2004. Distinctive image features from scale-invariant keypoints. *International Journal of Computer Vision*, **60**(2): 91−110.
[26] Bay, H., Ess, A., Tuytelaars, T., et al. 2008. Speeded-Up Robust Features (SURF). *Computer Vision and Image Understanding*, **110**(3): 346−359.
[27] Rublee, E., Rabaud, V., Konolige, K., et al. 2011. ORB: An efficient alternative to SIFT or SURF. In Proceedings of 2011 International Conference on Computer Vision.
[28] DeTone, D., Malisiewicz, T., Rabinovich, A. 2018. SuperPoint: Self-supervised interest point detection and description. *arXiv :1712.07629*.
[29] Sarlin, P. E., DeTone, D., Malisiewicz, T., et al. 2020. SuperGlue: learning feature matching with graph neural networks. *arXiv:1911.11763*.
[30] NASA SVS|Moon Phase and Libration. Available from https://svs.gsfc.nasa.gov/5187/ [Accessed 2025−02−24].
[31] Lunar/LROC: QuickMap. Available from https://quickmap.lroc.asu.edu [Aaccessed 2025−02−24].
[32] QuickMap. Available from https://www.actgate.com/products/quickmap [Accessed 2025−02−24].
[33] Robinson, M. S., Brylow, S. M., Tschimmel, M., et al. 2010. Lunar Reconnaissance Orbiter Camera (LROC) instrument overview. *Space Science Reviews*, **150**(1/4): 81−124.
[34] Zhou, Q., Li, X. 2019. STN-Homography: Direct estimation of homography parameters for image pairs. *Applied Sciences*, **9**(23): 5187.
[35] Wang, C. F. 2021. Research on homography transformation estimation based on convolutional neural network and its application. Master thesis, Zhengzhou University. (in Chinese)